Nonlinear Dyn
https://doi.org/10.1007/s11071-021-07073-z

ORIGINAL PAPER

Dynamic behavior of T-beam resonator with repulsive actuation

Yu Tian · Meysam Daeichin · Shahrzad Towfighian

Received: 5 April 2021 / Accepted: 13 November 2021

Abstract Electrostatic MEMS transducer driven by repulsive force is an attractive possibility and has advantages of avoiding the pull-in instability, tuning the natural frequency, and achieving high sensitivity by applying high enough voltages. In this work, a "T"-shaped beam, which is formed by attaching a secondary beam perpendicular to a primary cantilever at the tip, is introduced and its nonlinear dynamics is analyzed. A reduced-order model is derived from mode shapes formed from electromechanical coupling effects respectively. Generalized forms of forced Mathieu equation of motion are derived, and then, dynamic behaviors are investigated through the theory of multiple scales. The resonant responses, including both primary and principal parametric resonances, reveal softening behavior originating from quadratic and cubic nonlinearities in the governing equation. The behavior of the T-beam is compared with traditional cantilever structure. The resonance under repulsive force demonstrates that the T-beam has several advantages over a traditional cantilever: Lower natural frequency but higher resonant responses can improve the signal-to-noise ratio; with an attached micropaddle, the T-beam has a larger surface for absorption of targeted analytes for mass sensing. We conclude that an electrostatic MEMS resonator with a "T"-shaped beam is potentially appropriate for the new generations of sensors and actuators.

Keywords MEMS resonators · Repulsive force actuation · Nonlinear geometry · Primary resonances · Principal parametric resonances

Y. Tian · M. Daeichin · S. Towfighian (✉)
State University of New York at Binghamton, 4400 Vestal Parkway, Binghamton, NY 13902, USA
e-mail: stowfigh@binghamton.edu

Y. Tian
e-mail: ytian30@binghamton.edu

M. Daeichin
e-mail: mdaeich1@binghamton.edu

1 Introduction

Capacitive sensing and actuation have been the most common methods of transduction in MEMS transducers for the past few decades [1–3]. This transduction scheme is popular because of its compatibility with microfabrication technology, low sensitivity to temperature change, and small power consumption [1–3]. The basic design of this kind of transducers has not changed significantly since their introduction in 1970s and 1980s [4]. They are based on a two-electrode design such as parallel plate or comb-drive configurations. These designs suffer from pull-in instability [5], small stroke range [6], and low allowed voltages that hamper the sensitivity of these devices [4].

Repulsive electrode configuration is a multi-electrode capacitive scheme that addresses the pull-in issues associated with conventional two-electrode designs by producing significant out-of-plane actuation [7,8]. Since their introduction by Lee et al. [7], the nonlinear

Published online: 02 December 2021

dynamic behavior of this scheme has been extensively explored to produce different MEMS sensors and actuators such as micro-mirrors [9,10], microphones [11], accelerometers [12], MEMS switches [13], and resonators [8]. However, current designs of repulsive electrostatic MEMS transducers based on cantilever should be improved for applications needed for mass sensing.

A small surface area limits the performance in mass sensing. Generally, mass sensor measurements depend greatly on absorption/adsorption of the targeted analytes on and into sensing layer [14,15]. When certain molecules adhere to the surface, the change in deflection (static mass sensing) or resonant frequencies (dynamic mass sensing) can be measured [16–18] to determine the concentration of the targeted analytes. Tiny microbeams with limited attaching surface can only accommodate small amount of molecules which generates limited deflection and shift in resonant frequencies. To amplify the shift in the resonant frequency, microcantilevers are designed with a large surface area that contacts the targeted analytes. Larger surface area makes it possible for more molecules to adhere to the microstructure and therefore more significant change in the mass and resonance frequency. One of the common methods to increase the surface area is to attach a micropaddle to the microstructure [19–21].

To improve mass sensing capability, researchers have examined parametric resonance as an effective mechanism [22,23]. Unlike conventional MEMS mass sensors with high Q, which have to work in very low pressure and temperature to detect the small frequency shifts in resonance, parametrically excited MEMS oscillators measure the frequency shifts of the parametric resonance tongue. The transition from varying mass attachment at stability boundary is very distinct; therefore, tiny frequency changes can be detected with high resolution. The large responses of parametric resonators, unaffected by damping and without Q limitation, are ideal for high-resolution, highly sensitive mass sensors. Although there are many studies on the parametric resonance of gap-closing electrodes [24–27], there are just a few studies of parametric resonance of repulsive actuators [28,29].

To enhance mass sensing, we present a T-beam that has a larger surface area compared with cantilever system and study its fundamental and parametric resonances. The "T"-shaped beam is composed of a paddle at the free end of a microcantilever, driven by repulsive electrostatic configuration. Figure 1 shows the schematic of the T-beam MEMS resonator with dimensions and properties in Table 1. The electrostatic configuration (Fig. 2) consists of three separate electrodes. The first electrode is the movable T-beam. The second electrode is placed underneath the T-beam and is called the bottom electrode. The third electrode is a continuous side electrode that is placed on the substrate within a certain distance around the perimeter of the bottom electrode as shown in Fig. 1. Applying voltages on the side electrode while grounding the movable and bottom electrodes creates an electrostatic force on the movable electrode. This force is upward, meaning that it pushes the microstructure away from the bottom electrode [8,30]. The electrostatic force naturally eliminates the pull-in possibility between the movable and bottom electrodes [11,31]. Because the beam is pushed above its original position when a DC voltage is applied on the side electrode, the effective gap between the moving and bottom electrodes increases [8]. That provides more room for the vibration of the microstructure, enlarging its stroke [8,10,30].

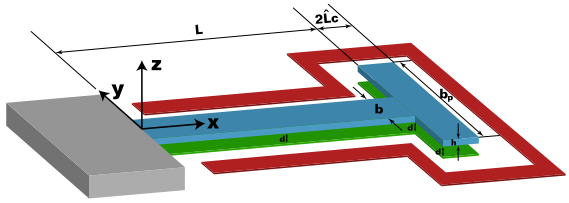

Fig. 1 Schematic of the T-beam repulsive force actuator assembly

The organization of the paper is as follows. Section 2 presents the derivation of the governing equation for a microcantilever with paddle that is subjected to repulsive electrode configuration. A lumped parameter model is extracted from the continuous governing equation of motion using Galerkin's decomposition method. The discretized equation resembles the nonlinear Mathieu's equation that is solved using the method of multiple scales. In Sect. 3, the static response of the microbeam to DC voltage excitation is obtained numerically with MATLAB. The dynamic response of the microstructure to DC+AC voltage excitation is investigated as well. The primary resonance and principal parametric resonance of the microstructure are analyzed and discussed in this section. Finally, Sect. 4 concludes the paper.

Table 1 Beam material and geometric properties

Parameter	Symbol	Value
Microbeam length (μm)	L	500
Micropaddle length (μm)	$2\hat{L}_c$	20
Microbeam width (μm)	b	20
Micropaddle width (μm)	b_p	200
Beam height (μm)	h	2
Beam electrode gap (μm)	d	2
Elastic modulus (GPa)	E	150
Density (kg/m^3)	ρ	2330
Poisson's ratio	ν	0.22
Force constant	p_9	-1.025×10^{34}
Force constant	p_8	2.635×10^{30}
Force constant	p_7	-2.895×10^{26}
Force constant	p_6	1.774×10^{22}
Force constant	p_5	-6.649×10^{17}
Force constant	p_4	1.576×10^{13}
Force constant	p_3	-2.387×10^{8}
Force constant	p_2	2.247×10^{3}
Force constant	p_1	-8.100×10^{-3}
Force constant	p_0	-1.043×10^{-7}
Force constant	r_9	-4.480×10^{33}
Force constant	r_8	1.186×10^{30}
Force constant	r_7	-1.346×10^{26}
Force constant	r_6	8.577×10^{21}
Force constant	r_5	-3.384×10^{17}
Force constant	r_4	8.622×10^{12}
Force constant	r_3	-1.436×10^{8}
Force constant	r_2	1.478×10^{3}
Force constant	r_1	-4.772×10^{-3}
Force constant	r_0	-8.767×10^{-8}

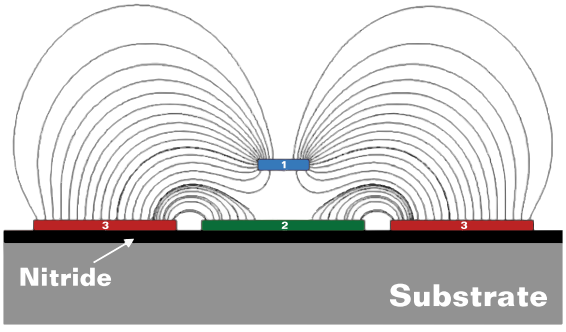

Fig. 2 Repulsive force electrode configuration with T-beam (1), fixed center electrode (2), and fixed side electrodes (3)

2 Problem formulation

The T-beam consists of two coupled beams: a primary microbeam fixed at one end with another shorter secondary microbeam attached at the tip. For reasonable simplification, when doing static and dynamic analyses, here we treat the structure as an Euler–Bernoulli beam (primary beam) of width b, thickness h , cross-sectional area $A_P = bh$, and second moment of area $I_P = \frac{1}{12}bh^3$. The micropaddle (secondary beam) is a rigid body with mass $\hat{M}$, mass moment of inertia $J = \frac{1}{12}\hat{M}(2\hat{L}_C)^2 = \frac{1}{3}\hat{M}\hat{L}_C^2$ around a line parallel to its width b_p passing through its center of mass.

2.1 Equation of motion

We derive the equation of motion for the system using the extended Hamilton's principle, shown in Eq. (1),

$$\int_{t_1}^{t_2} (\delta T_{total} - \delta U_{total} + \delta W_{NC})dt = 0 \tag{1}$$

where δT is the variation of kinetic energy, δU is the variation of potential energy, and δW_{NC} is the virtual work of nonconservative forces, such as damping. The beam-paddle hypothesis assumes the micropaddle is a rigid body and hardly contributes to the potential energy but significantly increases the kinetic energy [1]. The rotation angle θ_c is assumed equal to that of the microbeam (primary beam) tip $\hat{W}_{\hat{x}}(L, t)$. Here, the T-beam resonator system is treated as a conservative electromechanical system. The work done by the electrostatic forces on the T-beam is considered conservative and included in the potential energy. The virtual work done by nonconservative external force comes from viscous dissipation, mostly on the primary beam, and the portion on the secondary beam is neglected. The kinetic energy, potential energy, and virtual work for the microsystem are represented as Eqs. (2)–(8).

$$T_{prim} = \int_0^L \frac{1}{2}\rho A_P \dot{\hat{W}}^2(\hat{x}, \hat{t})d\hat{x} \tag{2}$$

$$T_{sec} = \frac{1}{2}\hat{M}[\dot{\hat{W}}(L, \hat{t}) + \hat{L_C}\dot{\hat{W}}_{\hat{x}}(L, \hat{t})]^2 + \frac{1}{2}J\dot{\hat{W}}_{\hat{x}}^2(L, \hat{t}) \tag{3}$$

$$T_{total} = T_{prim} + T_{sec} \tag{4}$$

$$U_{prim} = \int_0^L \frac{1}{2}EI_P\hat{W}_{\hat{x}\hat{x}}^2(\hat{x}, \hat{t})d\hat{x}$$

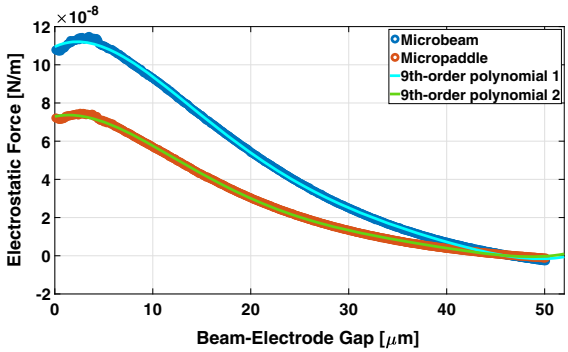

Fig. 3 Electrostatic force profile for T-beam actuator shown in Fig. 1

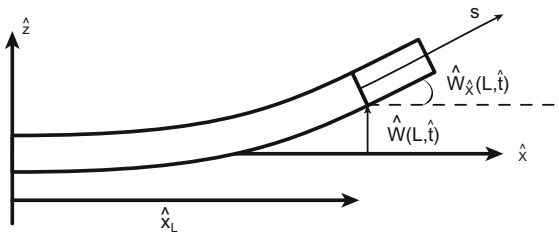

Fig. 4 Local coordinate system attached to the microplate

$$+\int_0^L V^2 f_1(\hat{W})\delta\hat{W}d\hat{x} \tag{5}$$

$$\begin{aligned}U_{sec} &= \int_0^{2\hat{L_C}} V^2\Big(f_2(\hat{W}+\hat{W}_{\hat{x}}s)\delta(\hat{W}+\hat{W}_{\hat{x}}s)\Big)\Big|_{\hat{x}=L} ds\\ &\approx \int_0^{2\hat{L_C}} V^2\Big(f_2(\hat{W})+f_2'(\hat{W})\hat{W}_{\hat{x}}s\Big)\delta(\hat{W}\\ &\quad +\hat{W}_{\hat{x}}s)\Big|_{\hat{x}=L} ds\\ &= V^2\Big(f_2(\hat{W})\times 2\hat{L_C}+f_2'(\hat{W})\hat{W}_{\hat{x}}\\ &\quad \times\frac{(2\hat{L_C})^2}{2}\Big)\Big|_{\hat{x}=L}\delta\hat{W}\\ &\quad +V^2\Big(f_2(\hat{W})\times\frac{(2\hat{L_C})^2}{2}+f_2'(\hat{W})\hat{W}_{\hat{x}}\\ &\quad \times\frac{(2\hat{L_C})^3}{3}\Big)\Big|_{\hat{x}=L}\delta\hat{W}_{\hat{x}}\end{aligned} \tag{6}$$

$$U_{total} = U_{prim} + U_{sec} \tag{7}$$

$$\delta W_{NC} = \int_0^L c\dot{\hat{W}}(\hat{x},\hat{t})\delta\hat{W}d\hat{x} \tag{8}$$

Table 2 Nondimensional substitutions

Parameter	Substitution
x-direction position	$x=\hat{x}/L$
W-direction position	$W=\hat{W}/h$
t-time	$t=\hat{t}/T$
ω-angular frequency	$\omega=\hat{\omega}\cdot T$
f-frequency	$f=\hat{f}\cdot T$
c-damping	$c=\hat{c}L^4/EIT$
Time constant	$T=\sqrt{\rho AL^4/EI}$
M-mass of paddle	$M=\hat{M}/\rho AL$
L_C-half length of paddle	$L_C=\hat{L_C}/L$
Force constant	$\alpha=L^4/EIh$
Force constant	$\kappa_1=2{L_C}^2\alpha$
Force constant	$\kappa_2=8L_C^3h\alpha/3$
Force constant	$\kappa_3=2L_C\alpha$
Force constant	$\kappa_4=2L_C^2h\alpha$

where $\hat{W}(\hat{x},\hat{t})$ is the z-direction beam displacement at location $\hat{x}$ and time $\hat{t}$ and s is a local coordinate attached to the microplate, as shown in Fig. 4. The subscript denotes the partial derivatives with respect to $\hat{x}$. d is the initial gap, V is the electrode voltage, and f_1, f_2 are referring to the electrostatic force on microbeam and micropaddle, respectively. Note that the first-order Taylor expansions are used when it comes to the nonlinear force on the paddle:

$$f_2(\hat{W}+\hat{W}_{\hat{x}}s)|_{\hat{x}=L}\approx f_2(\hat{W})|_{\hat{x}=L}+f_2'(\hat{W})\hat{W}_{\hat{x}}s|_{\hat{x}=L}.$$

The numerical profile for repulsive force is obtained and fit as two ninth-order polynomials from a finite element simulation for the intended fabrication dimensions in COMSOL (Fig. 3). The beam dimensions are listed in Table 1, and the nondimensional parameters are indicated in Table 2. Expressing and obtaining the variations of the energy terms and plugging them into Eq. (1) yield the nondimensionalized governing equation of motion for the system shown as

$$\ddot{W}+c\dot{W}+W_{xxxx}+\alpha V^2\sum_{i=0}^{9}p_ih^iW^i=0. \tag{9}$$

Boundary conditions are accordingly shown in Equations (10) for $x=0$ and Eqs. (11) and (12) for $x=1$,

$$W=0,\ W_x=0 \tag{10}$$

$$W_{xx}+ML_C\ddot{W}+\left(ML_C^2+\frac{M(2L_C)^2}{12}\right)\ddot{W}_x$$

$$+ V^2 \left(\kappa_1 \sum_{i=0}^{9} r_i h^i W^i + \kappa_2 W_x \sum_{i=0}^{8} r_{i+1} h^{i+1} W^i \right) = 0 \quad (11)$$

$$W_{xxx} - M\ddot{W} - L_C M \ddot{W}_x - V^2 \left(\kappa_3 \sum_{i=0}^{9} r_i h^i W^i + \kappa_4 W_x \sum_{i=0}^{8} r_{i+1} h^{i+1} W^i \right) = 0. \quad (12)$$

2.2 Mechanical mode shapes

Determining the microstructure's natural frequencies as accurately as possible is crucial for characterizing their actual geometry and boundary conditions, revealing their operating range and restrictions, and enabling accurate calibration of resonator-based devices [32]. By setting damping term $c = 0$ and forcing terms $V = 0$, linear eigenvalue problem is obtained:

$$\ddot{W} + W_{xxxx} = 0 \quad (0 \le x \le 1) \quad (13)$$

$$W_{xx} + ML_C\ddot{W} + \frac{4}{3}L_C^2 M \ddot{W}_x = 0 \quad (x = 1) \quad (14)$$

$$W_{xxx} - M\ddot{W} - L_C M \ddot{W}_x = 0 \quad (x = 1) \quad (15)$$

$$W = 0 \quad (x = 0) \quad (16)$$

$$W_x = 0 \quad (x = 0). \quad (17)$$

Using separation of variables $W(x,t) = \phi(x)q(t)$ and setting $\ddot{q}(t) = -\omega^2 q(t)$, where ω stands for the nondimensional natural frequency, the mode shape is written as

$$\phi(x) = c_1 cos(\beta x) + c_2 sin(\beta x) + c_3 cosh(\beta x) + c_4 sinh(\beta x) \quad (18)$$

where β is also a nondimensional parameter defined by $\omega = \beta^2$. Combining boundary conditions Eqs. (14)–(17), we can find $c_3 = -c_1$ and $c_4 = -c_2$, and the characteristic equation is described as

$$\begin{bmatrix} A & B \\ C & D \end{bmatrix} \begin{bmatrix} c_1 \\ c_2 \end{bmatrix} = \begin{bmatrix} 0 \\ 0 \end{bmatrix} \quad (19)$$

where

$$A = \beta^2(-cos(\beta) - cosh(\beta)) - ML_C\omega^2(cos(\beta) - cosh(\beta)) - \frac{4}{3}L_C^2 M\omega^2\beta(-sin(\beta) - sinh(\beta))$$

$$B = \beta^2(-sin(\beta) - sinh(\beta)) - ML_C\omega^2(sin(\beta) - sinh(\beta)) - \frac{4}{3}L_C^2 M\omega^2\beta(cos(\beta) - cosh(\beta))$$

$$C = \beta^3(sin(\beta) - sinh(\beta)) + M\omega^2(cos(\beta) - cosh(\beta)) + ML_C\omega^2\beta(-sin(\beta) - sinh(\beta))$$

$$D = \beta^3(-cos(\beta) - cosh(\beta)) + M\omega^2(sin(\beta) - sinh(\beta)) + ML_C\omega^2\beta(cos(\beta) - cosh(\beta)).$$

Table 3 Frequencies of the bending modes

Mode	ω	$\hat{f}$ (kHz)	c_2/c_1	$\hat{f}$ (COMSOL) (kHz)
1	2.1287	6.2779	−0.7776	6.2853
2	16.5657	48.854	−1.0110	48.846
3	49.9637	147.35	−0.9997	146.52
4	101.7657	300.12	−1.000	292.69

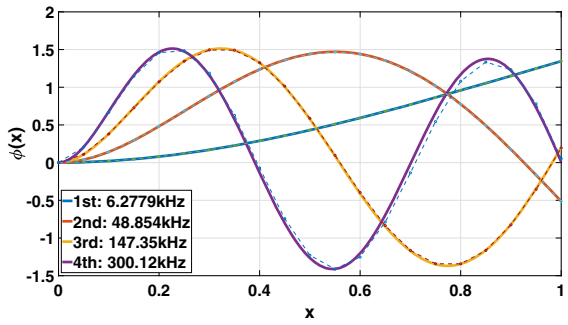

Fig. 5 First four mode shapes from MATLAB and COMSOL. Solid lines represent results from MATLAB, and dashed lines represent results from COMSOL

For eigenvalues and mechanical mode shapes, we need to obtain the nontrivial solutions to Eq. (19). Solving $\begin{vmatrix} A & B \\ C & D \end{vmatrix} = 0$ with MATLAB, values of β and c_2/c_1 for the first four mechanical modes are shown in Table 3, where the dimensional natural frequencies are calculated with $\hat{f} = \hat{\omega}/2\pi = \omega/(2\pi T) = \beta^2/(2\pi T)$. The results of modal frequencies are compared against COMSOL, which shows a close agreement (Figs. 5 and 6). Meanwhile, voltage-related boundary value problem is solved for mode shapes, but because of the significant nonlinearity from the microstructure as well as the electrostatics, several nonlinear terms have to be dropped in order to simplify the boundary value problem. Thus, the result is very close to that of our mechanical modal analysis and voltage-related modes

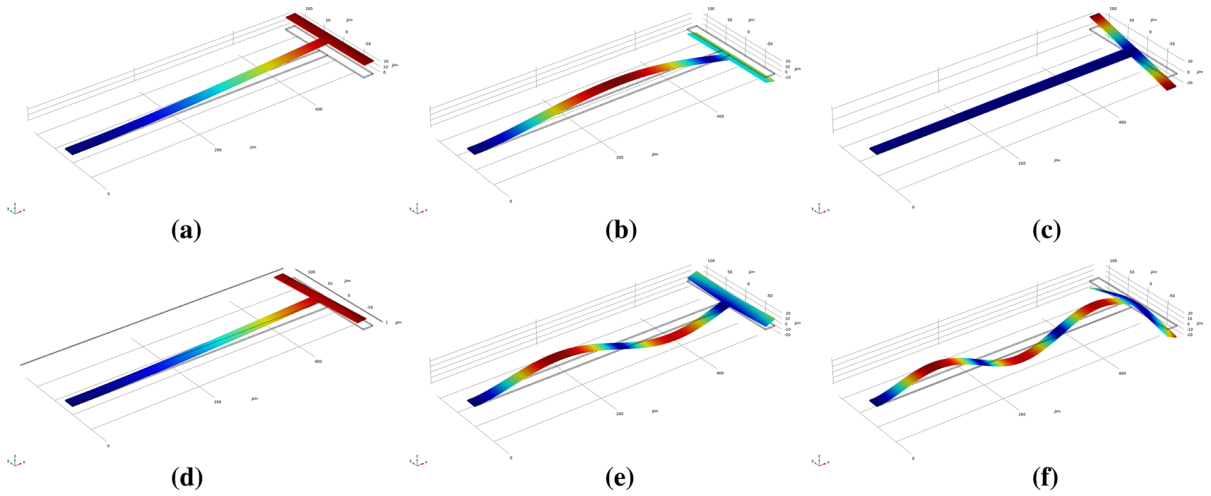

Fig. 6 Finite element simulations in COMSOL and the corresponding simulated modes: **a** First mode (frequency around 6.2853 kHz), **b** Second mode (frequency around 48.846 kHz), **c** Third mode (frequency around 49.592 kHz), **d** Fourth mode (frequency around 62.215 kHz), **e** Fifth mode (frequency around 146.52 kHz) and **f** Sixth mode (frequency around 292.69 kHz)

are not pursued. More details are included in Appendix A.

2.3 Reduced-order model

Once the mechanical modes shapes $\phi_m{}'s$ are known, with Galerkin's method, the partial differential equation in Eq. (1) is reduced to a set of ordinary differential equations (more details are included in Appendix B), Eq. (20), that can be solved numerically.

$$\begin{aligned}&\int_0^1 (\phi_m(x))(\sum_{j=1}^{N} \phi_j(x)\ddot{q}_j(t)\\&+ c\sum_{j=1}^{N}\phi_j(x)\dot{q}_j(t))dx + \sum_{j=1}^{N}\phi_j''''(x)q_j(t))dx\\&+\alpha V^2\sum_{i=0}^{9} p_i h^i \int_0^1 (\phi_m(x))\\&\sum_{j=1}^{N}(\phi_j(x)q_j(t))^i dx = 0\end{aligned} \tag{20}$$

where $m = 1, 2, ..., N$ and N represents the number of mode shapes in consideration.

For a one-mode approximation, Eq. (20) is reduced to,

$$\begin{aligned}&\int_0^1 (\phi_1(x))^2 dx\ddot{q}_1(t) + c\int_0^1 (\phi_1(x))^2 dx\dot{q}_1(t)\\&+\int_0^1 \phi_1(x)\phi_1''''(x)dx q_1(t)\\&+\alpha V^2\sum_{i=0}^{9} p_i h^i \int_0^1 (\phi_1(x))^{i+1}(q_1(t))^i dx = 0.\end{aligned} \tag{21}$$

2.4 Dynamic mathematical model

T-beam structure as a sensor or resonator is mostly utilized when resonating. The actuator voltage V that is applied to the structure becomes the input signal, which superimposes a sinusoidal function V_{AC} on the V_{DC} that operates the device. When applying the combination of two voltages,

$$\begin{aligned}V^2 &= (V_{DC} + V_{AC}cos\omega t)^2\\&= V_{DC}^2 + 2V_{DC}V_{AC}cos\omega t + \frac{(1+cos2\omega t)V_{AC}^2}{2}\end{aligned}$$

the term including V_{AC}^2 is dropped as well since the AC voltage is typically much smaller than DC voltage. Our efforts are then mostly focused on first-order resonance of the driving frequency, which accounts for the total displacement as

$$q_1(t) = q_{total}(t) = q_s + q(t) \tag{22}$$

where q_s stands for the static deflection and $q(t)$ represents the dynamic displacement. Our particular concerns are the dynamic response $q(t)$ about the static equilibrium position. Neglecting the squeeze-film damping as well as contact, a generalized form of forced Mathieu equation of motion is formulated as Eq. (23) based on one-mode approximation,

$$\begin{aligned}&\frac{\partial^2 q}{\partial \tau^2}+2\zeta\frac{\partial q}{\partial \tau}+(\omega_n^2+f_1\cos\Omega\tau)q\\&\quad+(\delta_2+f_2\cos\Omega\tau)q^2+(\delta_3+f_3\cos\Omega\tau)q^3\\&\quad+(\delta_4+f_4\cos\Omega\tau)q^4+(\delta_5+f_5\cos\Omega\tau)q^5\\&\quad+\ldots=F_0\cos\Omega\tau\end{aligned}\tag{23}$$

where

$$\tau=\omega_0 t,\ \Omega=\frac{\omega}{\omega_0},\ \zeta=\frac{c}{2\omega_0},$$

$$\omega_0=\sqrt{\frac{K_{11}}{M_{11}}},\ \omega_n=\sqrt{1+\delta_1}$$

with $\delta_j's$ and $f_j's$ resulting from DC voltage terms as described

$$M_{11}=\int_0^1(\phi_1(x))^2dx$$

$$K_{11}=\int_0^1\phi_1(x)\phi_1''''(x)dx$$

$$\delta_j=\frac{\alpha V_{DC}^2}{K_{11}}\sum_{i=j}^{9}\binom{i}{i-j}p_i h^i q_s^{i-j}\int_0^1(\phi_1(x))^{i+1}dx$$

$$F_0=\frac{-2\alpha V_{DC}V_{AC}}{K_{11}}\sum_{i=0}^{9}p_i h^i q_s^i\int_0^1(\phi_1(x))^{i+1}dx$$

$$f_j=\frac{2\alpha V_{DC}V_{AC}}{K_{11}}\sum_{i=j}^{9}\binom{i}{i-j}p_i h^i q_s^{i-j}\int_0^1(\phi_1(x))^{i+1}dx$$

where $\binom{n}{r}=\frac{n!}{(n-r)!r!}$. Before we apply the perturbation method, it is fundamental to keep linear terms while making nonlinear terms reasonably small. Here, the bookkeeping parameter ϵ is assumed to be at the order $O(10^{-2})$. The solved steady-state amplitude q_s, assumed of order $O(1)$, from Eq. (21) when $V=V_{DC}$, helps predict and assume the initial order of all the magnitude order of terms in Eq. (23) in Tables 4 and 5.

Based on theory of multiple scales in perturbation at most to the second order (ϵ^2 or T_2), the terms higher than that have really minimal effect on dynamic behavior, and therefore, we exclude the small nonlinearity of higher orders ($O(10^{-5})$ or smaller) and keep dynamic-related terms up to cubic terms. Equation (23) is reduced to,

$$\begin{aligned}&\ddot{q}+2\epsilon^2\zeta\dot{q}+(\omega_n^2+\epsilon f_1 cos\Omega\tau)q\\&\quad+\epsilon^2(\delta_2 q^2+f_2 q^2 cos\Omega\tau)\\&\quad+\epsilon^2(\delta_3+f_3 cos\Omega\tau)q^3+\epsilon^2(\delta_4+f_4 cos\Omega\tau)q^4\\&=\epsilon^2 F_0\cos\Omega\tau.\end{aligned}\tag{24}$$

We then seek an approximate asymptotic solution to Equation (24) by letting

$$\begin{aligned}q(\tau)=&\,q_0(T_0,T_1,T_2)+\epsilon q_1(T_0,T_1,T_2)\\&+\epsilon^2 q_2(T_0,T_1,T_2)+O(\epsilon^3)\end{aligned}\tag{25}$$

where $T_0=\tau$, $T_1=\epsilon\tau$ and $T_2=\epsilon^2\tau$ represent fast, slow and very slow timescale terms, respectively. For achieving solution to Eq. (24), it is essential to evaluate the conditions for primary and secondary resonances separately.

2.4.1 Primary resonance

Since the excitation F_0 is $O(\epsilon^2)$, $\Omega-\omega_n$ is assumed to be $O(\epsilon^2)$ for consistency. Hence, we introduce σ as detuning parameter examining the closeness of Ω to 1 by putting

$$\Omega=\omega_n+\epsilon^2\sigma.\tag{26}$$

Based on Table 4 (f_3, f_4, and higher ones are dropped), the governing Eq. (24) should be,

$$\begin{aligned}&\ddot{q}+2\epsilon^2\zeta\dot{q}+(\omega_n^2+\epsilon f_1 cos\Omega\tau)q\\&\quad+\epsilon^2(\delta_2 q^2+f_2 q^2 cos\Omega\tau)\\&\quad+\epsilon^2(\delta_3)q^3+\epsilon^2(\delta_4)q^4=\epsilon^2 F_0\cos\Omega\tau.\end{aligned}$$

To balance the effect of primary-resonance excitation, we need to reorder the equations so that the order of parametric and primary force and ζ all appears in the ϵ^2 order. Substituting Eqs. (25) and (27) into (24) and equating the coefficients of ϵ^0, ϵ^1 and ϵ^2 on both sides, we obtain

$$\epsilon^0:\ D_0^2 q_0+\omega_n^2 q_0=0\tag{27}$$

$$\epsilon^1:\ D_0^2 q_1+2D_0D_1q_0+\omega_n^2 q_1=0\tag{28}$$

$$\begin{aligned}\epsilon^2:\ &D_0^2 q_2+2D_0D_1q_1+(D_1^2+2D_0D_2)q_0+2\zeta D_0 q_0\\&+\omega_n^2 q_2+\delta_2 q_0^2+\delta_3 q_0^3+\delta_4 q_0^4\\&+f_1 q_0 cos\Omega\tau+f_2 q_0^2 cos\Omega\tau=F_0 cos\Omega\tau\end{aligned}\tag{29}$$

Table 4 The assumed order of magnitude for the terms shown in Eq. (23) for primary resonance with the values when V_{DC}=195V and V_{AC}=1.5V. f_3, f_4, and terms at higher order are dropped

Term	$\zeta\dot{q}$	$(1+\delta_1)q$	$f_1 q$	$\delta_2 q^2$	$f_2 q^2$	$\delta_3 q^3$	$f_3 q^3$	$\delta_4 q^4$	$f_4 q^4$	F_0
Order	$O(10^{-3})$	$O(1)$	$O(10^{-2})$	$O(10^{-2})$	$O(10^{-4})$	$O(10^{-4})$	$O(10^{-6})$	$O(10^{-4})$	$O(10^{-6})$	$O(10^{-1})$
T-beam	0.00385	1.8667	0.0133	−0.0315	−4.839e-4	−3.080e-4	−4.738e-6	2.266e-4	3.486e-6	0.147

Table 5 The assumed order of magnitude for the terms shown in Eq. (23) for principal parametric resonance with the values when V_{DC}=90V and V_{AC}=30V. Terms at higher order including f_5, δ_5 are dropped

Term	$\zeta\dot{q}$	$(1+\delta_1)q$	$f_1 q$	$\delta_2 q^2$	$f_2 q^2$	$\delta_3 q^3$	$f_3 q^3$	$\delta_4 q^4$	$f_4 q^4$	F_0
Order	$O(10^{-3})$	$O(1)$	$O(10^{-2})$	$O(10^{-3})$	$O(10^{-3})$	$O(10^{-3})$	$O(10^{-3})$	$O(10^{-4})$	$O(10^{-4})$	$O(1)$
T-beam	0.001	1.386	0.0225	4.186e-3	2.442e-3	−2.735e-3	−1.596e-3	2.162e-4	1.261e-4	3.0420

where $D_i = \frac{\partial}{\partial T_i}$. The general solution to Eq. (23) can be written in the form

$$q_0 = A(T_1, T_2)e^{i\omega_n T_0} + \bar{A}(T_1, T_2)e^{-i\omega_n T_0}. \tag{30}$$

Inserting Eq. (30) and (26) into Eqs. (28) and (29), eliminating the secular or resonance terms implies that

$$e^{i\omega_n T_0}\left\{\frac{f_2}{2}A^2 e^{-i\sigma T_2} + (f_2 A\bar{A} - \frac{F_0}{2})e^{i\sigma T_2} + 3\delta_3 A^2\bar{A} + 2i\omega_n(\zeta A + D_2 A)\right\} = 0. \tag{31}$$

Implementing polar notation of $A = \frac{1}{2}ae^{i\beta}$ in terms of amplitude a and nonlinear frequency β, introducing variable $\gamma = -\beta + \sigma T_2$, and separating real and imaginary parts give derivatives with respect to T_2 as

$$\gamma' = \frac{(-3f_2a^2 + 4F_0)cos\gamma - 3\delta_3 a^3 + 8a\omega_n\sigma}{8a\omega_n} \tag{32}$$

$$a' = \frac{(f_2a^2 + 4F_0)sin\gamma - 8a\omega_n\zeta}{8\omega_n}. \tag{33}$$

The analytical response for primary resonance is therefore represented as

$$q = a\cos(\beta + \omega_n\tau). \tag{34}$$

By setting right-hand side of Eqs. (32) and (33) to be zero for the asymptotic approximation, the amplitude a in terms of detuning parameter is determined by the equations:

$$\begin{cases}\lambda_1 cos\gamma + \lambda_3 = 0\\ \lambda_2 cos\gamma + \lambda_4 = 0.\end{cases}$$

The amplitude a is obtained by solving the simplified equation:

$$(\lambda_1\lambda_2)^2 = (\lambda_3\lambda_2)^2 + (\lambda_4\lambda_1)^2 \tag{35}$$

in which

$$\lambda_1 = 4F_0 - 3f_2a^2$$
$$\lambda_2 = 4F_0 - f_2a^2$$
$$\lambda_3 = 8a\sigma\omega_n - 3\delta_3 a^3$$
$$\lambda_4 = -8a\omega_m\zeta.$$

2.4.2 Principal parametric resonance

Here, the frequency of driving force is close to the systems natural frequency as

$$\Omega = 2\omega_n + \epsilon^2\sigma. \tag{36}$$

Based on Table 4 (f_5, δ_5, and higher ones are dropped), the governing Eq. (23) becomes

$$\ddot{q} + 2\epsilon^2\zeta\dot{q} + (\omega_n^2 + \epsilon f_1 cos\Omega\tau)q + \epsilon^2(\delta_2 q^2 + f_2 q^2 cos\Omega\tau) + \epsilon^2(\delta_3 + f_3 cos\Omega\tau)q^3 + \epsilon^2(\delta_4 + f_4 cos\Omega\tau)q^4 = \epsilon^2 F_0\cos\Omega\tau.$$

According to the reordering of ϵ^0, ϵ^1, and ϵ^2 in Eq. (24), we obtain

$$\epsilon^0 : D_0^2 q_0 + \omega_n^2 q_0 = F_0 cos\Omega T_0 \tag{37}$$

$$\epsilon^1 : D_0^2 q_1 + 2D_0 D_1 q_0 + \omega_n^2 q_1 = 0 \tag{38}$$

$$\epsilon^2 : D_0^2 q_2 + 2D_0 D_2 q_0 + 2\zeta D_0 q_0 + \omega_n^2 q_2 + \delta_2 q_0^2 + \delta_3 q_0^3 + \delta_4 q_0^4 + f_1 q_0 cos\Omega\tau + f_2 q_0^2 cos\Omega\tau + f_3 q_0^3 cos\Omega\tau + f_4 q_0^4 cos\Omega\tau = 0. \tag{39}$$

The general solution to Eq. (37) can be represented accordingly

$$q_0 = A(T_1, T_2)e^{i\omega_n T_0} + \bar{A}(T_1, T_2)e^{-i\omega_n T_0} + \Lambda(e^{i\Omega T_0} + e^{-i\Omega T_0}) \tag{40}$$

wherein $\Lambda = \frac{F_0}{2(\omega_n^2 - \Omega^2)}$. Eliminating the secular or resonance terms implies that

$$\begin{aligned} e^{i\omega_n T_0}\Big\{ & 2i\omega_n(\zeta A + D_2 A) + \frac{1}{2} f_1 \bar{A} e^{i\sigma T_2} \\ & + 2\delta_2 \Lambda \bar{A} e^{i\sigma T_2} + 2 f_2 A \Lambda + \delta_3 (3A^2 \bar{A} + 6A\Lambda^2) \\ & + \frac{f_3}{2}\left(A^3 e^{-i\sigma T_2} + 3A\bar{A}^2 e^{i\sigma T_2} + 9\Lambda^2 \bar{A} e^{i\sigma T_2} \right) \\ & + \delta_4 \Big(4A^3 \Lambda e^{-i\sigma T_2} + 12\Lambda^3 \bar{A} e^{i\sigma T_2} \\ & + 12A\bar{A}^2 \Lambda e^{i\sigma T_2} \Big) \\ & + f_4 \left(12\Lambda^3 A + 12\Lambda A^2 \bar{A} + 2\Lambda \bar{A}^3 e^{2i\sigma T_2} \right) \Big\} \\ = 0. & \end{aligned} \tag{41}$$

Implementing polar notation of $A = \frac{1}{2} a e^{i\beta}$ in terms of amplitude a and nonlinear frequency β, introducing variable $\gamma = -2\beta + \sigma T_2$, and separating real and imaginary parts give derivatives with respect to T_2 as

$$\begin{aligned} -8\omega_n \gamma' = & \Big(4 f_1 + 4 f_3 a^2 + 36 f_3 \Lambda^2 + 32\delta_4 \Lambda a^2 \\ & + 96\delta_4 \Lambda^3 + 16\delta_2 \Lambda \Big) cos\gamma + 4 f_4 \Lambda a^2 cos 2\gamma \\ & + 16 f_2 \Lambda + 96 f_4 \Lambda^3 + 24 f_4 \Lambda a^2 \\ & + 48\delta_3 \Lambda^2 + 6\delta_3 a^2 - 8\omega_n \sigma \end{aligned} \tag{42}$$

$$\begin{aligned} 16\omega_n a' = & -\Big(4 f_1 a + 36 f_3 \Lambda^2 a + 2 f_3 a^3 \\ & + 16\delta_4 \Lambda a^3 + 96\delta_4 \Lambda^3 a + 16\delta_2 \Lambda a \Big) sin\gamma \\ & - 4 f_4 \Lambda a^3 sin 2\gamma - 16\omega_n \zeta a. \end{aligned} \tag{43}$$

By setting right-hand side of Eqs. (42) and (43) to be zero for the asymptotic approximation, the amplitude a in terms of detuning parameter is determined by the equations:

$$\begin{cases} \lambda_5 cos\gamma + \lambda_6 cos 2\gamma + \lambda_7 = 0 \\ \lambda_8 cos\gamma + \lambda_9 cos 2\gamma + \lambda_{10} = 0 \end{cases}$$

in which

$$\begin{aligned} \lambda_5 &= 4 f_1 + 4 f_3 a^2 + 36 f_3 \Lambda^2 + 32\delta_4 \Lambda a^2 + 96\delta_4 \Lambda^3 \\ &\quad + 16\delta_2 \Lambda \\ \lambda_6 &= 4 f_4 \Lambda a^2 \\ \lambda_7 &= 16 f_2 \Lambda + 96 f_4 \Lambda^3 + 24 f_4 \Lambda a^2 + 48\delta_3 \Lambda^2 \\ &\quad + 6\delta_3 a^2 - 8\omega_n \sigma \\ \lambda_8 &= -\Big(4 f_1 a + 36 f_3 \Lambda^2 a + 2 f_3 a^3 + 16\delta_4 \Lambda a^3 \\ &\quad + 96\delta_4 \Lambda^3 a + 16\delta_2 \Lambda a \Big) \\ \lambda_9 &= -4 f_4 \Lambda a^3 \\ \lambda_{10} &= -16\omega_n \zeta a. \end{aligned}$$

The equations cannot be simplified like Eq. (35), and we can solve for a directly in the equations using Mathematica. The analytical response for principal parametric resonance is

$$q = a\cos(\beta + \omega_n \tau) + \frac{F_0}{\omega_n^2 - \Omega^2} \cos \Omega \tau. \tag{44}$$

3 Results and discussion

The static and dynamic behaviors of a T-beam resonator under repulsive force are mostly studied for a one-mode approximation model. The damping is estimated by

$$c = \frac{\beta_1^2}{Q}. \tag{45}$$

3.1 Static analysis

For the static analysis, the sensor voltage, V_s, is a constant DC voltage upwards of 200V. First, the boundary value problem is derived based on Eq. (9) after removing time-dependent components, which results in governing equation as Eq. (46):

$$W_s'''' + \alpha V_{DC}^2 \sum_{i=0}^{9} p_i h^i W_s{}^i = 0 \tag{46}$$

and the corresponding boundary conditions for $x = 0$ as Eq. (47) and for $x = 1$ as Eqs. (48) and (49):

$$W = 1, \; W' = 0 \tag{47}$$

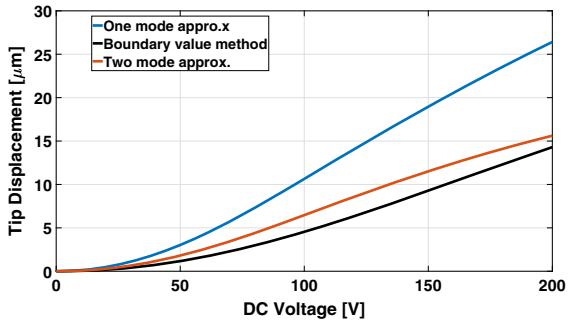

Fig. 7 Static equilibrium position of the end of primary beam as the DC voltage varies

$$W'' + V^2\Bigg(\kappa_1 \sum_{i=0}^{9} r_i h^i W^i + \kappa_2 W' \sum_{i=0}^{8} (i+1) r_{i+1} h^i W^i\Bigg) = 0 \tag{48}$$

$$W''' - V^2\Bigg(\kappa_3 \sum_{i=0}^{9} r_i h^i W^i + \kappa_4 W' \sum_{i=0}^{8} (i+1) r_{i+1} h^i W^i\Bigg) = 0. \tag{49}$$

The closed-form $W_s = W_s(x)$ that represents the static deflection is obtained using bvp4c in MATLAB after rewriting it to be four first-order ordinary differential equations. The solution $W_s(x)$ gives the static T-beam profile ($0 \leq x \leq 1$) for varying DC voltages. The tip deflection is then obtained for increasing DC voltages to capture the static solution shown in Fig. 7. Similar to previous research that revealed that electrostatic levitation could actuate the cantilever upward more than an order of magnitude larger than the initial gap [8,28], the T-beam is free from pull-in instability and can have a large stroke.

Moreover, removing the time-dependent terms in Eq. (20), the static deflections of the T-beam using mode approximations are also shown in Fig. 7. Comparison of results from boundary value method and reduced-order model implies that two-mode approximation is closer to the boundary value method. However, we compared the weight of each mode in Table 6. The values are normalized with respect to the total tip displacement. It is evident that weights of the first mode are always hundred times larger than the weights of the second mode. Because it is the dominant mode, we use the first mode approximation to obtain the dynamic responses.

The Jacobian matrix of Eq. (21) is computed at the static equilibrium points, and the corresponding eigenvalues of the Jacobian matrix yield the natural frequencies using a one-mode approximation at many voltages V_s in Fig. 8. T-beam resonator driven by repulsive force shows relatively small natural frequency, while it produces a high deflection (Fig. 7). Merging T-beam and electrostatic levitation as one single MEMS mass sensor, therefore, enables detecting a small change in the resonant frequency with less susceptibility to noise. The merger can inspire a new generation of mass sensors using the phenomenon of mode localization [32] by connecting two single resonators with a coupling beam. Meanwhile, the T-beam undoubtedly enlarges the surface which helps detect and measure the presence of different kinds of analytes, including biological species like viruses or bacteria, whether in liquid or gaseous media or specific gases, especially volatile organic compounds (VOCs).

3.2 Perturbation analysis

The method of multiple scales (MMS) perturbation technique is applied to perturb the microactuator near its fundamental natural frequency and at twice that frequency to numerically solve the governing equations accordingly and study the actuator's primary and principal parametric resonant behaviors. With σ serving as a detuning parameter and the nondimensional amplitude a, we can investigate more than dynamic T-beam responses by comparing them with cantilevers under the same excitation. For determining the steady-state response amplitudes in the vicinity of the principal parametric resonance, the stability of periodic motions is examined by determining the relevant eigenvalues of the Jacobian matrix in the vicinity of the periodic motions. A positive eigenvalue represents an unstable limit circle in phase portrait, and even slight disturbance leads to boundless increasing amplitudes. This effect does not happen if the eigenvalue is negative, which helps the disturbance decay with time. When analyzing primary resonance, a stable displacement of the T-beam can be reflected by the stable amplitude a. Unstable amplitudes are hard to hold. For principal parametric resonance, things get much intriguing. When amplitude a in our solution (Eq. (44)) is associ-

Table 6 Normalized weights of each mode in two-mode approximation

DC Voltage [V]	0	20	40	60	80	100	120	140	160	180	200
$\frac{\phi_1 q_1}{\phi_1 q_1 + \phi_2 q_2}$	0	1.0051	1.0051	1.0052	1.0055	1.0059	1.0065	1.0072	1.0081	1.0091	1.0102
$\frac{\phi_2 q_2}{\phi_1 q_1 + \phi_2 q_2}$	0	−0.0051	−0.0051	−0.0052	−0.0055	−0.0059	−0.0065	−0.0072	−0.0081	−0.0091	−0.0102

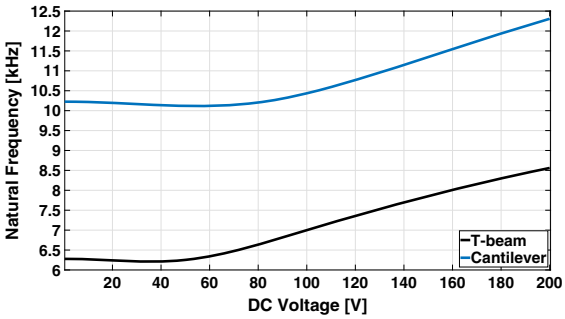

Fig. 8 First natural frequency of the beam as the DC voltage varies

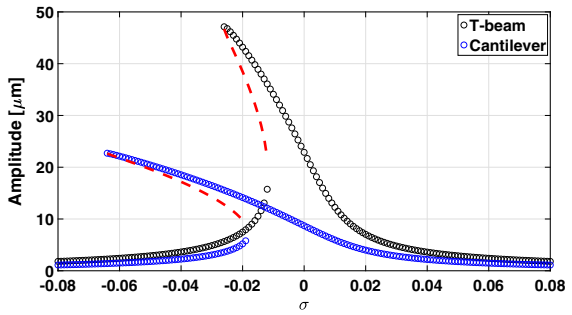

Fig. 9 Comparison of primary resonant response at $V_{DC} = 195V$ and $V_{AC} = 1.5V$ for T-beam and cantilever. Quality factor is set to 130. Markers (black circle for T-beam and blue circle for cantilever) indicate amplitude of stable responses, and dashed red lines represent unstable branch

ated with a negative eigenvalue, the response is defined as principal parametric resonance because the response period is the same as the excitation period. However, when the eigenvalue has a positive sign, it indicates subharmonic resonance. Parametric resonance has a much larger amplitude than subharmonic resonance, which is why most researchers on MEMS resonators see opportunities. In order to study the advantages of utilizing T-shaped beam instead of traditionally applied cantilever, which is highly popular and widely integrated into MEMS sensing due to the well-known excellent properties, in designing the resonator under repulsive configuration, we can compare T-beam's dynamic behaviors with cantilever of same dimensions, meaning 500 microns in length and 20 microns in width. Then, a great potential to improve new generations of sensors and actuators by combining T-beam and electrostatic levitation appears.

3.2.1 Primary resonance

Comparing with results of a cantilever of the same length in primary resonance in Fig. 9, we conclude that the dynamic response of T-beam also shows hysteresis and softening behavior, which is because of a quadratic term and a negative cubic term for the electrostatic force from the forcing profile polynomial fit. These two terms are dominant in the forcing function and explain why the softening is significant even at AC voltage near 1.5V. That means, as the frequency approaches the natural frequency, the oscillation amplitude increases significantly, and when the frequency drops below the resonant frequency, the system experiences hysteresis and drops to a significantly smaller oscillation amplitude. To validate the results, we make a comparison of the primary resonance obtained from the perturbation, long-time integration, and shooting methods [1] as depicted in Fig. 10. All of them are based on Eq. (21) with one-mode approximation. As it is deduced, the perturbation method overestimates the results, which has been reported in previous studies of nonlinear resonators [33]. However, it is a computationally efficient and quick method to roughly estimate the response of the system. For more accurate responses, shooting technique is recommended.

3.2.2 Principal parametric resonance

In general, the parametric excitation actuation is more efficient, requires less voltages than the primary resonance excitation, and makes the response faster as the excitation frequency is twice the resonance. Figure 11 demonstrates that the T-beam's parametric resonance

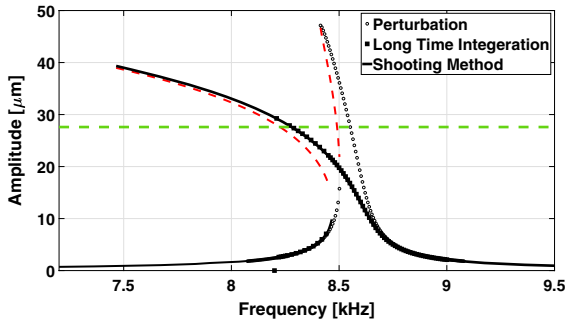

Fig. 10 Simulation results of primary resonant response at $V_{DC} = 195V$ and $V_{AC} = 1.5V$ for T-beam comparing perturbation, long-time integration, and shooting methods. Quality factor is set to 130. Markers (circle for perturbation and square for long time integration) and solid black lines (for shooting method) indicate the amplitude of stable responses. Dashed red lines represent unstable branches, and the dashed green line indicates the approximate threshold amplitude at which the beam tip will hit the substrate

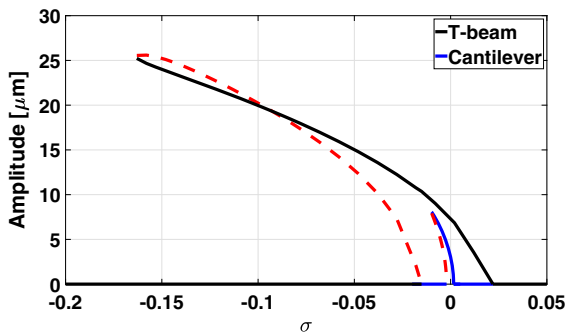

Fig. 11 Comparison of principal parametric resonant response at $V_{DC} = 90V$ and $V_{AC} = 10V$ for T-beam and cantilever. Quality factor is set to 500. Solid lines (black for T-beam and blue for cantilever) indicate the amplitude of stable responses, and dashed red lines represent unstable branch

achieves a much higher amplitude than the cantilever. The quality factor for parametric resonance is set to 500 to avoid high AC voltages to trigger parametric resonance. At very low quality factors, parametric resonance is not activated or requires very high AC voltages. At large amplitudes, the beam hovers around the bottom electrode, but does not collide with it because of the squeeze film damping effect as our previous study reported [28]. Because of electrostatic levitation, the usable range of dynamics is now about 25 μm compared to 2 μm of the initial gap, which is a significant range of motion for micro-actuators.

The T-beam resonator can achieve very large dynamic amplitudes from parametric resonance as shown in

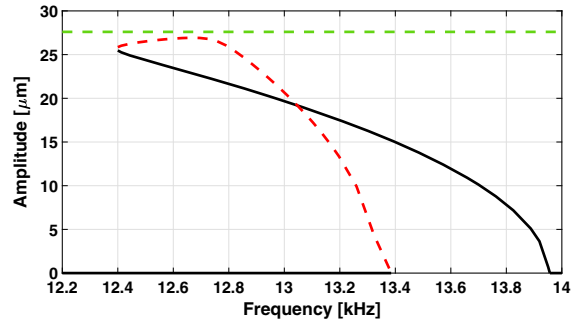

Fig. 12 Principal parametric resonance of T-beam resonator at $V_{DC} = 90V$ and $V_{AC} = 30V$. Quality factor is set to 500. The solid black lines indicate amplitude of stable responses. The dashed red line represents the unstable branch, and the dashed green line indicates the approximate threshold amplitude at which the beam tip will hit the substrate

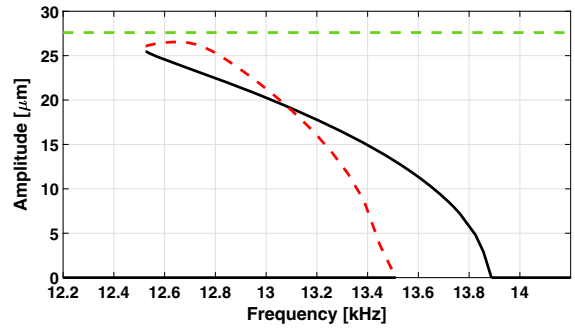

Fig. 13 Principal parametric resonance of T-beam resonator at $V_{DC} = 90V$ and $V_{AC} = 20V$. Quality factor is set to 500. The solid black lines indicate amplitude of stable responses. The dashed red line represents the unstable branch, and the dashed green line indicates the approximate threshold amplitude at which the beam tip will hit the substrate

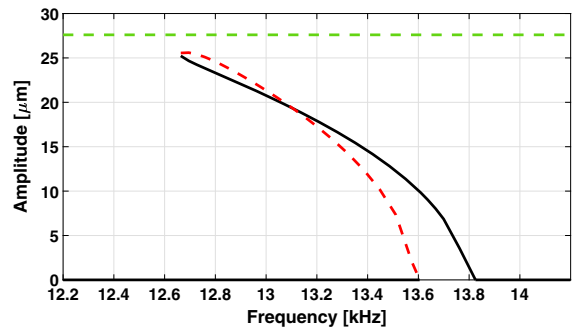

Fig. 14 Principal parametric resonance of T-beam resonator at $V_{DC} = 90V$ and $V_{AC} = 10V$. Quality factor is set to 500. The solid black lines indicate amplitude of stable responses. The dashed red line represents the unstable branch, and the dashed green line indicates the approximate threshold amplitude at which the beam tip will hit the substrate

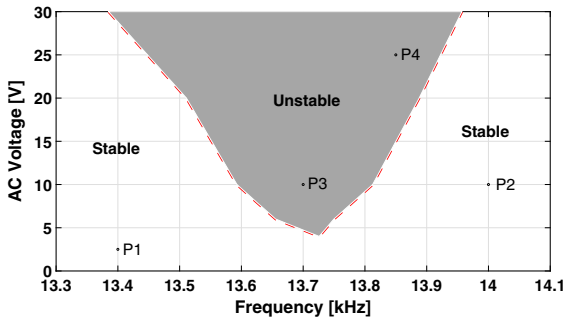

Fig. 15 Transition curve for principal parametric resonance of T-beam resonator at $V_{DC} = 90V$. Quality factor is set to 500

Figs. 12, 13, and 14 . If the AC voltage is high enough, the unstable branch, which is indicated in red, intersects the stable branch, which is indicated in black. The intersection of stable and unstable branches is called transcritical bifurcation where the two branches exchange stability. In fact, the bifurcations in generalized parametric resonance have been thoroughly investigated [24] and the bifurcation diagram shown here, describing physically achievable amplitudes without hitting the substrate, is a type of the quasi-softening nonlinear characteristics. Based on the simulation, an AC voltage of at least 4V is necessary to overcome the threshold voltage for parametric resonance when the DC voltage is 90V and the quality factor is 500. Since the perturbation method is computationally fast, especially in vicinity of targeted frequency range, and can predict both stable and unstable branches, it can also be applied to produce the principal parametric transition curve shown in Fig. 15. The unstable area (grey area) is where the parametric resonance happens, while in the stable area (white area), only quasi-periodic happens. This transition curve shows a minimum threshold voltage of about $V_{AC} = 4V$ when quality factor is 500. The responses at four points (P1, P2, P3, and P4) in Fig. 15 are shown in Fig. 16 to better indicate whether the beam is showing parametric resonance or quasi-periodic motion. Inlets of Fig. 16 show more detailed waveforms of oscillation over 20 excitation periods. It is evident that the oscillation amplitudes of parametric

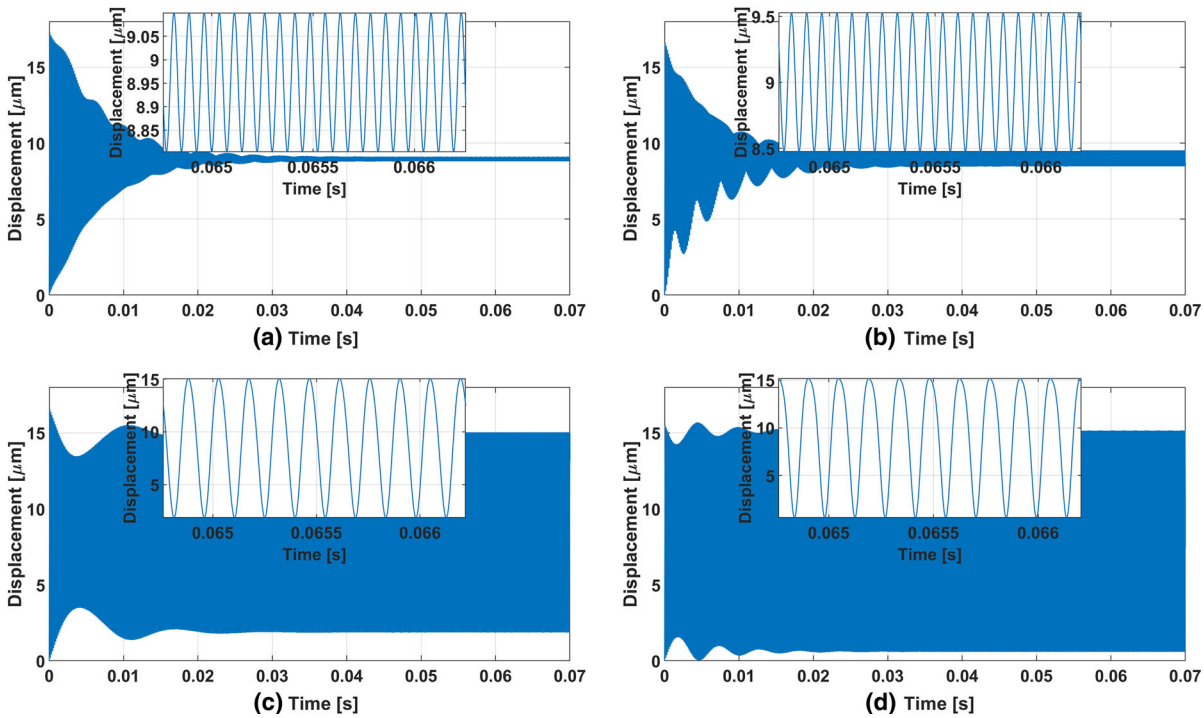

Fig. 16 Time responses of four points in Fig. 15 when $V_{DC} = 90$V: (a) P1 ($V_{AC} = 2.5$V, $f_{excitation} = 13.4$kHz, $f_{oscillation} = 13.4$kHz), (b) P2 ($V_{AC} = 10$V, $f_{excitation} = 14$kHz, $f_{oscillation} = 14$kHz), (c) P3 ($V_{AC} = 10$V, $f_{excitation} = 13.7$kHz, $f_{oscillation} = 6.85$kHz), (d) P4 ($V_{AC} = 25$V, $f_{excitation} = 13.85$kHz, $f_{oscillation} = 6.925$kHz)

resonance (P3 and P4) are much bigger than that of quasi-periodic motion (P1 and P2); for parametric resonance, the oscillation period is the twice the excitation period, while for quasi-periodic motion, the oscillation period is the same as the excitation period. It can be easily seen that there are 20 peaks in inlets of P1 and P2 and 10 peaks in inlets of P3 and P4.

The T-beam's ability to achieve unprecedented amplitudes is highly advantageous for resonance sensors where a large signal-to-noise ratio is desired. The DC voltage governs the center frequency, which provides tunability for the proposed system without pull-in instability. This is in contrast to parallel-plate devices that the increase in DC voltage makes the system prone to pull-in collapse.

Future work can investigate internal resonance because the T-beam enables having commensurate relationships between modal frequencies. This property can be very useful for filtering and mass sensing.

4 Conclusion

A MEMS mass sensor prototype of an electrostatic T-beam under the influence of a repulsive force is presented in this paper. The proposed model for approximation uses an Euler–Bernoulli beam with a rigid paddle attached to the tip. Analytical and numerical responses were obtained. These results show that it is possible to predict the upper bound of the primary and parametric resonances using a one-mode approximation. The comparison made with cantilever under same conditions shows better properties, including higher amplitude in oscillation of primary and principal parametric resonance, which contributes to large signal-to-noise ratios and enhanced resolutions. Especially in principal parametric resonance, the significantly greater amplitude than cantilever beam gives much promising applications combining research achievements in this area. We have also presented the transition curve to specify the region where the system shows distinct large parametric resonances. The fact that the presented repulsive resonator does not suffer from pull-in instability and has large amplitudes makes it suitable for optical sensors and actuators to achieve high resolution. The T-beam resonator can improve the next generations of mass sensors to have better sensitivity.

Acknowledgements The authors would like to acknowledge the financial support of this study by National Science Foundation (NSF) through grant CMMI 1919608.

Data availability All data generated or analyzed during this study are included in this published article.

Declarations

Conflict of interest The authors declare that they have no conflict of interest.

Appendix

A. Derivation of voltage-related modes

Using Galerkin's method to discretize, we approximate the beam deflection as:

$$W(x,t)\approx W_s(x)+\sum_{j=1}^{n}\phi(x)q(t),\ \ddot{q}(t)=-\omega^2 q(t). \tag{50}$$

In our case, the mode shape for a T-beam is of the form:

$$\phi(x)=c_1\cos(\beta x)+c_2\sin(\beta x)+c_3\cosh(\beta x)+c_4\sinh(\beta x) \tag{51}$$

in which we have $\omega=\beta^2$.

Plug into boundary conditions and combine them with $W_s(x)$: @$x=0$:

$$\phi(x)q(t)=0\Rightarrow c_1+c_3=0 \tag{52}$$

$$\phi'(x)q(t)=0\Rightarrow c_2+c_4=0 \tag{53}$$

@x=1:

$$\begin{aligned}&\phi''(x)q(t)+ML_C\phi(x)\ddot{q}(t)+\frac{4}{3}ML_C^2\phi'(x)\ddot{q}(t)\\&+V^2\kappa_1\sum_{i=0}^{9}r_i h^i\left([W_s(x)+\phi(x)q(t)]^i-[W_s(x)]^i\right)\\&+V^2\kappa_2\Bigg([W_s'(x)+\phi'(x)q(t)]\sum_{i=0}^{8}r_{i+1}h^{i+1}[W_s(x)\\&+\phi(x)q(t)]^i\\&-W_s'(x)\sum_{i=0}^{8}r_{i+1}h^{i+1}[W_s(x)]^i\Bigg)=0\end{aligned} \tag{54}$$

$$\begin{aligned}&\phi'''(x)q(t)-M\phi(x)\ddot{q}(t)-ML_C\phi'(x)\ddot{q}(t)\\&-V^2\kappa_3\sum_{i=0}^{9}r_i h^i\left([W_s(x)+\phi(x)q(t)]^i-[W_s(x)]^i\right)\end{aligned}$$

$$- V^2\kappa_4\Bigg([W_s'(x)+\phi'(x)q(t)]\sum_{i=0}^{8} r_{i+1}h^{i+1}[W_s(x)+\phi(x)q(t)]^i - W_s'(x)\sum_{i=0}^{8} r_{i+1}h^{i+1}[W_s(x)]^i\Bigg) = 0. \tag{55}$$

Simplify the above to be:
@x=1:

$$\phi''(x)q(t) - \omega^2 ML_C\phi(x)q(t) - \frac{4}{3}\omega^2 ML_C^2\phi'(x)q(t) + V^2\kappa_1\sum_{i=0}^{9} r_i h^i\left([W_s(x)+\phi(x)q(t)]^i - [W_s(x)]^i\right) + V^2\kappa_2 W_s'(x)\sum_{i=0}^{8} r_{i+1}h^{i+1}\times \tag{56}$$

$$\left([W_s(x)+\phi(x)q(t)]^i - [W_s(x)]^i\right) + V^2\kappa_2\phi'(x)q(t)\sum_{i=0}^{8} r_{i+1}h^{i+1}\times \tag{57}$$

$$\left[W_s(x)+\phi(x)q(t)\right]^i = 0 \tag{58}$$

$$\phi'''(x)q(t) + \omega^2 M\phi(x)q(t) + \omega^2 ML_C\phi'(x)q(t) - V^2\kappa_3\sum_{i=0}^{9} r_i h^i\left([W_s(x)+\phi(x)q(t)]^i - [W_s(x)]^i\right) - V^2\kappa_4 W_s'(x)\sum_{i=0}^{8} r_{i+1}h^{i+1}\times \tag{59}$$

$$\left([W_s(x)+\phi(x)q(t)]^i - [W_s(x)]^i\right) - V^2\kappa_4\phi'(x)q(t)\sum_{i=0}^{8} r_{i+1}h^{i+1} \times \left[W_s(x)+\phi(x)q(t)\right]^i \tag{60}$$

$$= 0. \tag{61}$$

Drop nonlinear terms of $\phi(x)q(t)$ and $q(t)$ is canceled:
@x=1:

$$\phi''(x) - \omega^2 ML_C\phi(x) - \frac{4}{3}\omega^2 ML_C^2\phi'(x) + V^2\kappa_1\phi(x)\sum_{i=1}^{9} r_i h^i\binom{i}{1}[W_s(x)]^{i-1} + V^2\kappa_2 W_s'(x)\phi(x)\sum_{i=1}^{8} r_{i+1}h^{i+1}\binom{i}{1}[W_s(x)]^{i-1} + V^2\kappa_2\phi'(x)r_1 h = 0 \tag{62}$$

$$\phi'''(x) + \omega^2 M\phi(x) + \omega^2 ML_C\phi'(x) - V^2\kappa_3\phi(x)\sum_{i=1}^{9} r_i h^i\binom{i}{1}[W_s(x)]^{i-1} - V^2\kappa_4 W_s'(x)\phi(x)\sum_{i=1}^{8} r_{i+1}h^{i+1}\binom{i}{1}[W_s(x)]^{i-1} - V^2\kappa_4\phi'(x)r_1 h = 0. \tag{63}$$

Table 7 Voltage-related mode shapes

DC Voltage [V]	0	20	40	100	200
β	1.4590	1.45906	1.45923	1.46264	1.47572
c_2/c_1	0.77758	0.77757	0.77753	0.77667	0.77346

The algebraic equations above can be solved, and therefore, voltage-related natural frequencies are obtained as given in Table 7. They are quite close to each other, most probably from dropping too many nonlinear terms, and both static and dynamic results based on them hardly have any difference.

B. Derivation of Mathieu's equation [Eq. (23)] based on one-mode approximation

One mechanical mode approximation is applied after checking the voltage-related modes. From static deflection q_s, we have:

$$\int_0^1 \phi_1(x)\phi_1''''(x)dx q_s + \alpha(V_{DC}^2)\sum_{i=0}^{9} p_i h^i\int_0^1(\phi_1(x))^{i+1}(q_s)^i dx = K_{11}q_s + \alpha(V_{DC}^2)\sum_{i=0}^{9} p_i h^i\int_0^1(\phi_1(x))^{i+1}(q_s)^i dx = 0. \tag{64}$$

Plug $V^2 = V_{DC}^2 + 2V_{DC}V_{AC}cos\omega t$ and $q_1(t) = q_{total}(t) = q_s + q(t)$ into Eq. (21):

$$\begin{aligned}
&\int_0^1 (\phi_1(x))^2 dx\ddot{q}(t) + c\int_0^1 (\phi_1(x))^2 dx\dot{q}(t) \\
&\quad + \int_0^1 \phi_1(x)\phi_1''''(x)dx(q_s + q(t)) \\
&\quad + \alpha(V_{DC}^2)\sum_{i=0}^{9} p_i h^i \int_0^1 (\phi_1(x))^{i+1}(q_s + q(t))^i dx \\
&\quad + \alpha(2V_{DC}V_{AC}cos\omega t) \\
&\quad \times \sum_{i=0}^{9} p_i h^i \int_0^1 (\phi_1(x))^{i+1}(q_s + q(t))^i dx \qquad (65) \\
&= M_{11}\ddot{q}(t) + 2\zeta\omega_0 M_{11}\dot{q}(t) + K_{11}(q_s + q(t)) \\
&\quad + \alpha(V_{DC}^2) \times \sum_{i=0}^{9} p_i h^i \int_0^1 (\phi_1(x))^{i+1} dx(q_s + q(t))^i \\
&\quad + \alpha(2V_{DC}V_{AC}cos\omega t) \\
&\quad \times \sum_{i=0}^{9} p_i h^i \int_0^1 (\phi_1(x))^{i+1} dx(q_s + q(t))^i = 0.
\end{aligned}$$

Subtract Eq. (64) from (65) and do some manipulating with respect to $\tau = \omega_0 t$:

$$\begin{aligned}
&{\omega_0}^2\ddot{q}(\tau) + 2\zeta\omega_0 \times \omega_0\dot{q}(\tau) + \frac{K_{11}}{M_{11}}(q(\tau)) \\
&\quad + \frac{\alpha}{M_{11}}(V_{DC}^2 + 2V_{DC}V_{AC}cos\frac{\omega}{\omega_0}\tau)\sum_{i=0}^{9} p_i h^i \\
&\quad \times \int_0^1 (\phi_1(x))^{i+1}(q_s + q(\tau))^i dx \qquad (66) \\
&\quad - \frac{\alpha}{M_{11}}(V_{DC}^2)\sum_{i=0}^{9} p_i h^i \int_0^1 (\phi_1(x))^{i+1}(q_s)^i dx = 0.
\end{aligned}$$

Finally, rearranging based on order of $(q(t))^k (k = 0, 1, 2, ...)$ in the expansion of $(q_s + q(t))^i$ and manipulating the equation with respect to $q(\tau) = q(\omega_0 t)$, we will get Eq. (23).

References

1. Younis, M.I.: MEMS linear and nonlinear statics and dynamics. Springer, New York (2011)
2. Rahmanian, S., Hosseini-Hashemi, S., Rezaei, M.: Out-of-plane motion detection in encapsulated electrostatic MEMS gyroscopes: principal parametric resonance. Int. J. Mech. Sci. (2020). https://doi.org/10.1016/j.ijmecsci.2020.106022
3. Babatain, W., Bhattacharjee, S., Hussain, A.M., Hussain, M.M.: Acceleration sensors: sensing mechanisms, emerging fabrication strategies, materials, and applications. ACS Appl. Electron. Mater. **3**(2), 504 (2021)
4. Miles, R.N.: A compliant capacitive sensor for acoustics: avoiding electrostatic forces at high bias voltages. IEEE Sens. J. **18**(14), 5691 (2018)
5. Zhang, W., Yan, H., Peng, Z., Meng, G.: Electrostatic pull-in instability in MEMS/NEMS: a review. Sens. Actuators A Phys. **214**, 187–218 (2014). https://doi.org/10.1016/j.sna.2014.04.025
6. He, S., Mrad, R.B.: Large-stroke microelectrostatic actuators for vertical translation of micromirrors used in adaptive optics. IEEE Trans. Ind. Electron. **52**(4), 974 (2005)
7. Lee, K., Cho, Y.H.: Laterally driven electrostatic repulsive-force microactuators using asymmetric field distribution. J. Microelectromech. Syst. **10**, 128 (2001). https://doi.org/10.1109/84.911101
8. Pallay, M., Daeichin, M., Towfighian, S.: Dynamic behavior of an electrostatic MEMS resonator with repulsive actuation. Nonlinear Dyn. **89**(2), 1525 (2017)
9. He, S., Mrad, R.B.: Design, modeling, and demonstration of a MEMS repulsive-force out-of-plane electrostatic micro actuator. J. Microelectromech. Syst. **17**(3), 532 (2008)
10. Ozdogan, M., Daeichin, M., Ramini, A., Towfighian, S.: Parametric resonance of a repulsive force MEMS electrostatic mirror. Sens. Actuators A Phys. **265**, 20 (2017)
11. Ozdogan, M., Towfighian, S., Miles, R.N.: Modeling and characterization of a pull-in free MEMS microphone. IEEE Sens. J. **20**(12), 6314 (2020)
12. Daeichin, M., Ozdogan, M., Towfighian, S., Miles, R.: Dynamic response of a tunable MEMS accelerometer based on repulsive force. Sens. Actuators A Phys. **289**, 34 (2019)
13. Pallay, M., Miles, R.N., Towfighian, S.: A tunable electrostatic MEMS pressure switch. IEEE Trans. Ind. Electron. **67**(11), 9833 (2019)
14. Jaber, N., Ilyas, S., Shekhah, O., Eddaoudi, M., Younis, M.I.: Multimode excitation of a metal organics frameworks coated microbeam for smart gas sensing and actuation. Sens. Actuators A Phys. **283**, 254 (2018)
15. Henriksson, J., Villanueva, L.G., Brugger, J.: Ultra-low power hydrogen sensing based on a palladium-coated nanomechanical beam resonator. Nanoscale **4**, 5059 (2012)
16. Battiston, F., Ramseyer, J.P., Lang, H., Baller, M., Gerber, C., Gimzewski, J., Meyer, E., Güntherodt, H.J.: A chemical sensor based on a microfabricated cantilever array with simultaneous resonance-frequency and bending readout. Sens. Actuators B Chem. **77**(1–2), 122 (2001)
17. Bouchaala, A., Jaber, N., Shekhah, O., Chernikova, V., Eddaoudi, M., Younis, M.: A smart microelectromechanical sensor and switch triggered by gas. Appl. Phys. Lett. **109**, 013502 (2016). https://doi.org/10.1063/1.4955309
18. Jaber, N., Ilyas, S., Shekhah, O., Eddaoudi, M., Younis, M.I.: In: 2018 IEEE Sensors, pp. 1–4 (2018)
19. Nayfeh, A.H., Quakad, H.M., Najar, F., Choura, S., Abdel-Rahman, E.M.: Nonlinear dynamics of a resonant gas sensor. Nonlinear Dyn. **59**, 607 (2010)
20. Krylov, S., Maimon, R.: Pull-in dynamics of an elastic beam actuated by continuously distributed electrostatic force. ASME. J. Vib. Acoust **126**(3), 332–342 (2004)

21. Rabih, A.A., Dennis, J., Ahmed, A., Khir, M.M., Ahmed, M.G., Idris, A., Mian, M.U.: MEMS-based acetone vapor sensor for non-invasive screening of diabetes. IEEE Sens. J. **18**(23), 9486 (2018)
22. Zhang, W., Baskaran, R., Turner, K.L.: In: ASME International Mechanical Engineering Congress and Exposition, vol. 36428, pp. 121–125 (2002)
23. Moran, K., Burgner, C., Shaw, S., Turner, K.: A review of parametric resonance in microelectromechanical systems. Nonlinear Theory Appl. IEICE **4**(3), 198 (2013)
24. Rhoads, J.F., Shaw, S.W., Turner, K.L., Moehlis, J., DeMartini, B.E., Zhang, W.: Generalized parametric resonance in electrostatically actuated microelectromechanical oscillators. J. Sound Vib. **296**(4–5), 797 (2006)
25. Rhoads, J.F., Shaw, S.W., Turner, K.L.: The nonlinear response of resonant microbeam systems with purely-parametric electrostatic actuation. J. Micromech. Microeng. **16**(5), 890 (2006)
26. DeMartini, B.E., Rhoads, J.F., Turner, K.L., Shaw, S.W., Moehlis, J.: Linear and nonlinear tuning of parametrically excited MEMS oscillators. J. Microelectromech. Syst. **16**(2), 310 (2007)
27. Prakash, G., Raman, A., Rhoads, J., Reifenberger, R.G.: Parametric noise squeezing and parametric resonance of microcantilevers in air and liquid environments. Rev. Sci. Instrum. **83**(6), 065109 (2012)
28. Pallay, M., Towfighian, S.: A parametric electrostatic resonator using repulsive force. Sens. Actuators A Phys. **277**, 134 (2018)
29. Pallay, M., Daeichin, M., Towfighian, S.: Feasibility study of a micro-electro-mechanical-systems threshold-pressure sensor based on parametric resonance: experimental and theoretical investigations. J. Micromech. Microeng. **31**(2), 025002 (2020)
30. Daeichin, M., Miles, R.N., Towfighian, S.: Experimental characterization of the electrostatic levitation force in MEMS transducers. J. Vib. Acoust. **142**(4), 041008 (2020)
31. Daeichin, M., Miles, R., Towfighian, S.: Lateral pull-in instability of electrostatic MEMS transducers employing repulsive force. Nonlinear Dyn. **100**(3), 1927 (2020)
32. Rabenimanana, T., Walter, V., Kacem, N., Le Moal, P., Bourbon, G., Lardies, J.: Mass sensor using mode localization in two weakly coupled MEMS cantilevers with different lengths: design and experimental model validation. Sens. Actuators A Phys. **295**, 643 (2019)
33. Yang, W., Towfighian, S.: A hybrid nonlinear vibration energy harvester. Mechan. Syst. Signal Process. **90**, 317 (2017)